ELSEVIER

Catalysis Today 58 (2000) 151–166

CATALYSIS TODAY

www.elsevier.com/locate/cattod

II–VI semiconductors made by soft chemistry
Syntheses and optical properties

M.P. Pileni

Laboratoire SRSI, URA CNRS 1662, Universite P. et M. Curie Bât F, 4 Place Jussieu, 75005 Paris, France

Abstract

In the present paper we give an overview of the effect of syntheses on the optical properties of II–VI semiconductors made in reverse micelles. This concerns CdS, CdTe and alloys such as $Cd_{1-y}Mn_yS$, $Cd_{1-y}Zn_yS$. © 2000 Elsevier Science B.V. All rights reserved.

Keywords: II–VI semiconductors; Synthesis and optical properties; CdS; CdTe

1. Introduction

The fabrication of assemblies of perfect nanometer-scale crystallites (quantum crystal), identically replicated in unlimited quantities in such a state that they can be manipulated and understood as pure macromolecular substances, is an ultimate challenge of modern materials research with outstanding fundamental and potential technological consequences. These potentialities are mainly due to the unusual dependence of the electronic properties on the particle size, either for metal [1–4] or semiconductor [1,5–18] or diluted magnetic semiconductor [19–26] particles, in 1–10 nm range.

Nanometer-size crystals exhibit behavior intermediate between bulk material and molecule. Their sizes range from smaller to a few times larger than the effective Bohr diameter of an exciton in bulk crystal. These systems have been paid special attention because of their unique size-dependent properties which include optical properties such as absorption and third-order nonlinearity as well as solar energy. Since the size dependence of the band levels of semiconductor particles results in a shift of optical spectrum, quantum mechanical descriptions of the shift were carried out by several researchers [6–8,14–19,27].

An important II–VI semiconductor quantum dot is CdTe because of its larger exciton Bohr diameter (15 nm). It has received some attention and its bandgap shift with cluster size has been well mapped [28–35]. Usually the CdTe quantum dots are made by RF magnetron sputtering in a glass matrix [28–35].

Type II–VI diluted magnetic semiconductors (DMS) [36] are semiconductors, where host cations (II) are randomly substituted by magnetic ions, Mn^{2+}. The presence of localized magnetic ions in a semiconductor alloy leads to exchange interactions between s–p band electrons and the Mn^{2+} d electrons. This sp–d exchange interaction constitutes a unique interplay between semiconductor physics and magnetism. It plays a double role in determining optical properties:

1. The bandgap of the compound is altered depending upon the concentration of manganese ions.
2. The 3d levels of transition metal ions are located in the bandgap region and d–d transitions dominate the spectrum.

E-mail address: pileni@sri.jussieu.fr (M.P. Pileni)

0920-5861/00/$ – see front matter
PII: S0920-5861(00)00250-9

In the nanometer-size crystallites of semimagnetic semiconductors, many of these properties are expected to be influenced by the quantum confinement of the electronic states and to be different from those of the bulk crystals. Due to the quantum dots unique properties, these nanostructures have a great potential for a variety of applications. Recent work on manganese-doped nanocrystals suggests that doped nanocrystals are a new class of materials [21].

2. Experimental

2.1. Products

Sodium di(ethyl-2-hexyl) sulfosuccinate, Na(AOT) was obtained from Sigma and sodium sulfide (Na_2S) from Janssen. The solvents isooctane, isopentane and methylcyclohexane were obtained from Fluka, ethanol from Prolabo, heptane and dodecanethiol from Merck. Cadmium and manganese di(ethyl-2-hexyl) sulfosuccinate [$Cd(AOT)_2$ and $Mn(AOT)_2$] was synthesized in our laboratory as described previously [37].

2.2. Apparatus

Photoluminescence spectra were recorded with a Spex fluorolog (1681). An Oxford cryostat with a controller (ITC502) was used to control the sample temperature (77–300 K). Optical absorption spectra were obtained with a Cary (1E) and HP 8452A UV–Vis spectrophotometer.

Energy dispersive spectrometry (EDS) measurements were made with a Link AN 10000. A Jeol (100 kV) model JEM 100CX II was used for transmission electron microscopy (TEM) and electron diffraction. The mean diameter, D_m, and the standard deviation, σ_m, were derived from an average number of 500 particles.

The EPR data were obtained using BRUKER ER 080 (200/60) spectrometers operating at 9.5 GHz (X-bands) for $103\,K<T<298\,K$.

3. Synthesis of disodium telluride, Na_2Te

In the synthesis by soft chemistry disodium telluride, Na_2Te is prepared first. It has to be mentioned that this product is highly poisonous and oxidizable. To make Na_2Te we used the two procedures described in [38]. The difference of these two is based mainly on the reaction time and on the amount of naphthalene used as catalyst. One of the procedures gives disodium telluride containing large amount of impurities. The only procedure suitable for making pure Na_2Te is described below. The reaction is carried out under nitrogen atmosphere by using standard Schlenk technique. A Schlenk is charged with tellurium powder (48 mmol), sodium (96 mmol), naphthalene (0.8 mmol) and 20 ml of tetrahydrofuran, THF, which has been distilled and degassed previously by freeze-thaw process under nitrogen. The reaction mixture is stirred for 4 days at room temperature and filtered. The product is washed with 20 ml of fresh degassed THF and dried under vacuum. Na_2Te is then in powder form which can be easily oxidized. So, the procedure described below to make CdTe nanoparticles is done in glass box.

4. Syntheses and control parameters

II–VI semiconductors are synthesized using reverse micelles [39]. Coprecipitation takes place on mixing two micellar solutions having the same water content, $w=[H_2O]/[AOT]$: 0.1 M Na(AOT) containing either S^{2-} or Te^{2-} ions, and a mixed micellar solution made of Na(AOT) and the reactants as $Cd(AOT)_2$, $Zn(AOT)_2$, $Mn(AOT)_2$. The syntheses are made at various x ratio with $x=([Cd^{2+}]+[Mn^{2+}])/[Te^{2-}]$ or $x=([Cd^{2+}]+[Mn^{2+}])/[S^{2-}])$.

After mixing the two micellar solutions, the procedure differs as follows:

- Procedure I: Dodecanethiol is immediately added to the micellar solution having a given water content, w. This results in a selective surface reaction between the thio derivative and cadmium and manganese ions. The particles are extracted immediately from micelles and the surfactant is removed by ethanol addition. The nanocrystallites coated by dodecanethiol are dispersed in a mixture of two solvents (isopentane–methylcyclohexane, 3 (v/v)) forming an optically clear glass at low temperature. The average size of coated particles increases upon increasing the water content in the medium in which the particles are synthesized.

- Procedure II. The particles are left in the micellar solution for 48 h. Dodecanethiol is then added and the particles are immediately extracted.
- Procedure III. Immediately after synthesis, dodecanethiol is added and the nanocrystallites remain in the micellar solution for 48 h. Then, the particles are extracted from micelles by using the same procedure as described above.
- Procedure IV. Nanocrystallites are kept in the micellar solution for 90 min and then dodecanethiol is added and the particles are extracted as described above.

For all the samples prepared, the composition, y, is determined by EDS. The nanocrystal structure is determined from electron diffraction. The particle size, determined from TEM pattern, is controlled by the size of the water droplets in which syntheses are made. Similar behavior has been observed for various nanoparticles [1]. As expected, the aging of particles (procedure II) induces an increase in the particle size compared to what is observed by procedure I.

5. Cadmium telluride nanocrystals [40]

Syntheses are made at various water content under procedures I and II. To prevent the oxidation of telluride, the syntheses were made in the presence of an excess of cadmium (x=[Cd^{2+}]/[Te^{2-}]=2). Table 1 gives the average particle size and the size distribution for the two procedures used. Hence procedure I permits a change in the particle size from 2.6 to 3.4 nm whereas it is from 3.4 to 4.1 nm by procedure II.

Electron diffraction studies confirmed that the CdTe nanocrystallites exhibited the bulk-like, zinc blende crystal structure. The coated particles are analyzed by EDS; they are composed of 51% of Cd and 49% of Te. The electron diffraction, the EDS and the average size distribution (13%), remain unchanged with the various procedures used (I and II) and for various particle sizes.

As observed for direct semiconductors, the CdTe absorption spectrum is size-dependent. Figs. 1 and 2 show a red shift in the absorption spectrum upon increasing the water content and then upon increasing the particle size. This is attributed to a quantum size effect [6–8,14–19,27–35]. The energy bandgap is deduced from the first derivative of the absorption spectrum. Table 1 gives the values of the energy bandgap determined by these two methods and for the various procedures (I and II). It increases with decreasing CdTe particle size. When comparison is possible, Table 1 shows an unchanged value of the bandgap with the synthesis mode. However, the excitonic peak is better defined for particles produced by procedure II than I (Fig. 1B and A). It has to be noticed that the absorption spectra of particles differing by their sizes and preparation modes present a shoulder at 750 nm which cannot be attributed to oxide formation. Preliminary EXAFS data confirm the absence of oxide. This is valid in the range of error of the experimental data. Hence, no obvious explanations can be given to explain this.

The photoluminescence (PL) spectra markedly change with the procedure used. Figs. 2A, C and E show a long tail PL spectrum. This is due to the recombination of charge carriers in the surface traps [32,41]. At the opposite, Figs. 2B, D, F show a well

Table 1
Average diameter, D (nm), of CdTe nanoparticles obtained at various water in oil droplet sizes, d (nm) and through the two procedures, σ (%) is the size distribution

	d (nm)		
	1.5	3	12
Procedure I			
D (nm)	2.6	3.1	3.4
σ (%)	17.8	13.2	11.6
E_g (1) (eV)[a]	1.99	1.96	1.92
E_g (2) (eV)	2.17	2.07	2.02
Procedure II			
D (nm)	3.4	3.8	4.1
σ (%)	12.7	11.9	11.1
E_g (1) (eV)	1.92	1.89	1.81
E_g (2) (eV)	2.02	1.97	1.87
ω_{PL} (300 K) (eV)	2.04	1.99	–
E_g (77 K) (eV)[b]	2.07	2.01	1.89
ω_{PL} (77 K) (eV)[c]	2.09	2.03	1.91
Φ_{PL}[d]	1	0.98	0.11

[a] E_g (1) and E_g (2) are the energy bandgap determined either from [$\sigma h\nu=(h\nu-E_g)^{1/2}$] or from the first derivation of the absorption spectrum at 300 K.

[b] E_g (77 K) is the energy bandgap determined at 77 K.

[c] ω_{PL} (300 K) and ω_{PL} (77 K) are the PL peak position at 300 and 77 K.

[d] The relative fluorescence quantum yield, determined at 77 K, is Φ_{PL}.

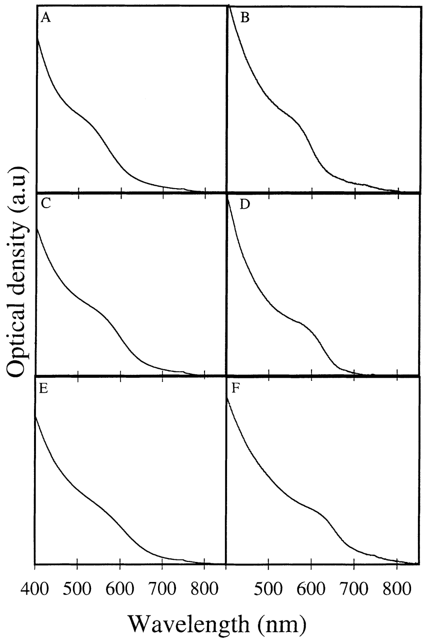

Fig. 1. Absorption spectra of CdTe nanocrystals made at various water content: A and B (w=5), C and D (w=10), E and F (w=20). A, C and E are made by procedure I and B, D and F are made by procedure II. $x=[\mathrm{Te}^{2-}]/[\mathrm{Cd}^{2+}]=\frac{1}{2}$.

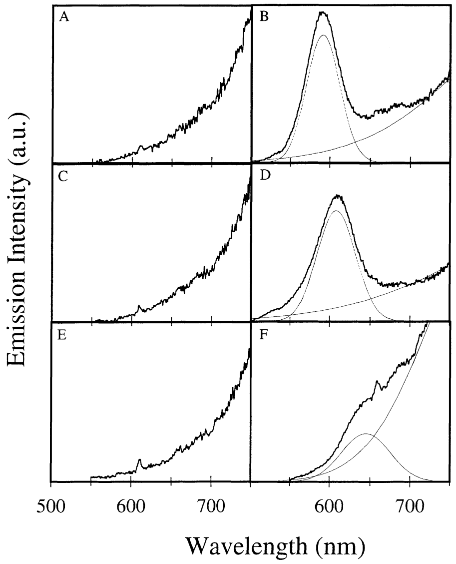

Fig. 2. PL spectra of CdTe nanocrystals made at various water content and recorded at 77 K: A and B (w=5), C and D (w=10), E and F (w=20). A, C and E are made by procedure I and B, D and F are made by procedure II. $x=[\mathrm{Te}^{2-}]/[\mathrm{Cd}^{2+}]=\frac{1}{2}$.

defined peaks centered at higher energies. Assuming that this spectrum is due to the sum of two PL spectra which are described by two Gaussians, the photoluminescence maximum at high energy, recorded at 300 K, ω_{PL}(300 K) and 77 K, ω_{PL}(77 K), are deduced. The energy bandgap and the maximum of photoluminescence are very close (Table 1). This permits to attribute the photoluminescence at higher energy to the direct recombination of free electron and hole. Table 1 shows a red shift in the maximum of the PL spectrum due to the direct transition by increasing the particle size. This is due to a quantum size effect. Comparison of the PL peak position and the band edge measured from absorption shows they are very close (Table 1). This confirms that the PL peak observed at high energy arises from the recombination of a free electron and hole. The relative fluorescence quantum yield of the direct transition, Φ_{PL}, is obtained by assuming two Gaussian curves (one due to the direct transition and second due to trap emissions). Table 1 shows a decrease in the quantum yield, Φ_{PL}, upon increasing the particle size. From a comparison of the PL spectra obtained with particles differing by their sizes and their fabrication modes, it is possible to conclude that the aging permits to observe the direct transition. This can be explained by formation of a passivated layer due to Oswald ripening which permits to decrease the surface defects and then the trap emissions. These data have to be related to those obtained with CdSe previously. The CdSe nanoparticles are produced through inorganic syntheses at 280°C. A direct transition is observed, at room temperature, when the particles are coated by ZnS. This has been explained by a decrease in the number of CdSe defects with shell formation. Similarly direct transition has been observed by adsorbate addition at the particle interface. The procedure described permits to obtain the direct transition without addition of external adsorbate. This is the first time that, by using reverse micelles, the direct transition is observed.

6. Cadmium sulfide nanocrystals

In our previous work [4,9,18,27] the synthesis of CdS has been done by using the procedure I. In these cases no direct fluorescence was observed. To check if the direct fluorescence of CdS could be observed by using procedure II and in the presence of an excess of cadmium (x=[Cd^{2+}]/[S^{2-}]=2), syntheses of CdS nanocrystals are performed in the same experimental conditions as described above (syntheses at various water contents). Fig. 3 shows, as expected, a shift toward low energy when the average size of particles increases. As observed with CdTe the excitonic peak is better resolved when the particles are aged. This is probably due to better crystalinity. The PL spectra of CdS nanocrystals differing by their sizes and their fabrications are very broad and correspond to CdS defect states [5,9,18,42,43] (Fig. 4). Hence, as opposed to what is observed with CdTe, the aging does not permit to obtain the direct fluorescence of CdS. However, we know that when the syntheses are made in an excess of cations, this increases the sulfur vacancies and then the trap emission as observed (Fig. 4). So to prevent the presence of sulfur vacancies, syntheses have been made in the presence of excess sulfur (x=[Cd^{2+}]/[S^{2-}]=$\frac{1}{2}$). Fig. 5 shows a large PL spectrum due to the trap emission. However, a peak is observed at lower energy and is attributed to the direct transition. Hence the aging permits to observe the direct transition of sulfur rich CdS nanocrystals.

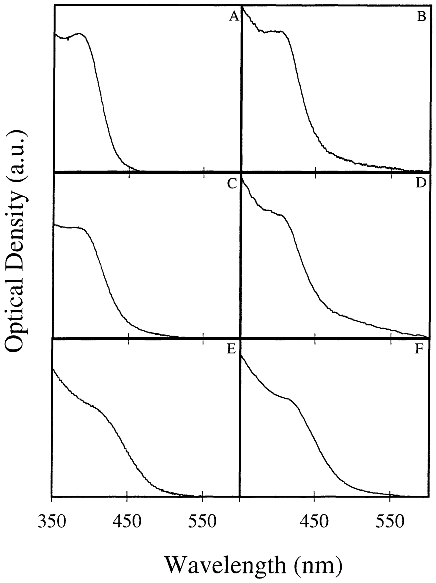

Fig. 3. Absorption spectra of CdS nanocrystals made at various water content: A and B (w=5), C and D (w=10), E and F (w=20). A, C and E are made by procedure I and B, D and F are made by procedure II. x=[S^{2-}]/[Cd^{2+}]=$\frac{1}{2}$.

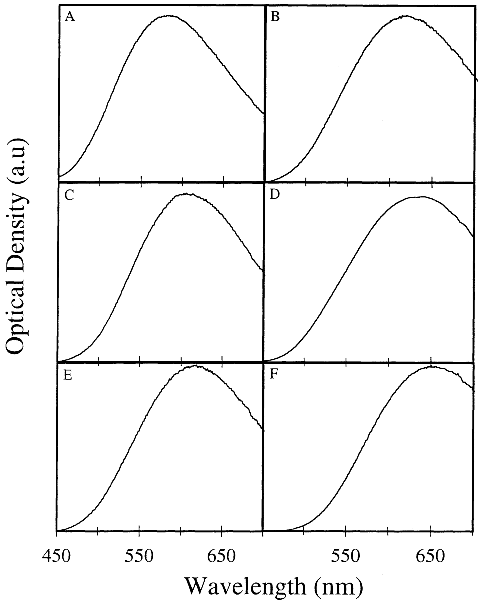

Fig. 4. PL spectra of CdS nanocrystals made at various water content: A and B (w=5), C and D (w=10), E and F (w=20). A, C and E are made by procedure I and B, D and F are made by procedure II. x=[S^{2-}]/[Cd^{2+}]=$\frac{1}{2}$.

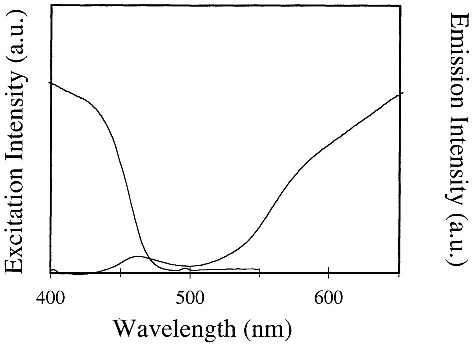

Fig. 5. Excitation and PL spectra of 4 nm CdS nanocrystals prepared by procedure III. x=[S^{2-}]/[Cd^{2+}]=2.

7. II–VI semiconductors alloys

7.1. *Solid solution of $Cd_{1-y}Zn_yS$ [44–46]*

As expected, the absorption spectrum of $Cd_{1-y}Zn_yS$ particles made under procedure I and having the same composition, y, is red shifted on increasing the particle size. At fixed size, the red shift in the absorption spectrum with increasing composition is observed. This is due to changes in the solid phase composition. The energy bandgap, determined from the excitonic peak, smoothly increases with increasing composition from ZnS to CdS (Table 2). Similar behavior was observed for the bandgap variation of bulk $Cd_{1-y}Zn_yS$ [47]. Solid solution is obtained when syntheses are made in the presence of an excess of sulfur ($x=([Cd^{2+}]+[Zn^{2+}])/[S^{2-}]=\frac{1}{2}$).

7.2. Solid solution of $Cd_{1-y}Mn_yS$ [48–53]

As for $Cd_{1-y}Zn_yS$, syntheses of $Cd_{1-y}Mn_yS$ nanocrystals are made in the presence of an excess of sulfur ($x=\frac{1}{2}$). In the presence of an excess of cations, no solid solutions are obtained. The nanoparticles are characterized by a zinc blende structure, whereas the bulk phase has a wurtzite structure. A similar change in the structure between the bulk phase and nanocrystals is observed for CdS [44,54].

The syntheses are made by using procedure I. As already observed, the size of the coated particles increases on increasing the micellar water content of reverse micelles. For a fixed composition, a red shift in the absorption spectrum with increasing particle size is observed (Fig. 6A). This is a direct result of the quantum confinement effects [5–18]. For a given average particle diameter, the absorption spectrum differs with composition, y (Fig. 6B).

From the absorption spectra, the direct bandgap is determined from the absorption onset. For a given composition, there is an increase in the band edge energy upon decreasing the particle size as shown in Fig. 6C. This is due to the quantum size effect.

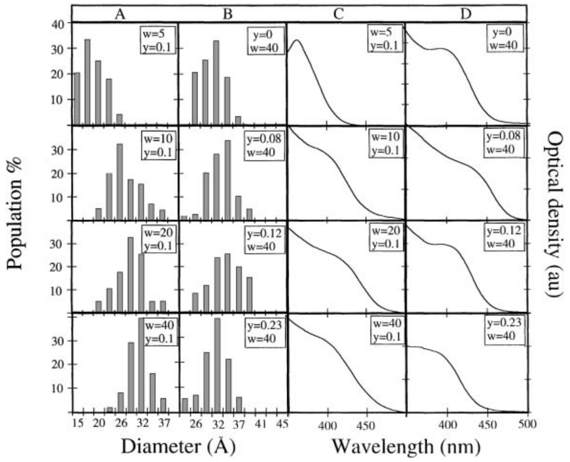

Fig. 6. Size distribution and absorption spectra of $Cd_{1-y}Mn_yS$ particles synthesized at various water contents (w=0–40) and various manganese concentrations (y=0–0.23).

For a given particle size, the bandgap does not vary monotonically with composition, as is observed for most semiconductor alloys. It decreases and then increases (Fig. 7). Similar behavior has been observed in the bulk phase [55] and films [56]. With nanocrystals, the minimum is more pronounced and its depth increases with decreasing particle size (Fig. 7).

Table 2
Variation of the energy bandgap, E_g (eV) with particle size and composition

y (%)	Diameters (nm)		
	2	2.3	2.9
0	4.20	4.16	3.97
25	3.60	3.46	3.26
50	3.32	3.22	2.97
75	3.16	3.06	2.76
100	3.10	2.99	2.67

The appearance of the minimum in the energy bandgap with increasing composition, y, could be attributed to a chemical disorder which is usually attributed to a shift of the energy levels due to statistical fluctuations of the crystal potential in an alloy and called bandgap bowing. It has been described, for the

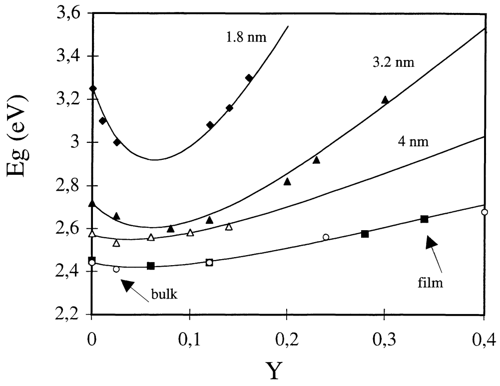

Fig. 7. Variation of the bandgap energy, E_g, with composition, y, for various particles size, bulk and thin film. The line is obtained from the best fit between experimental data and Eq. (2).

bulk phase, by [56]

$$E_g(y,T) = E_{g(\mathrm{CdS})} + \Delta E y - cy(1-y) \quad (1)$$

where $E_{g(\mathrm{CdS})}$ and ΔE are the band edge energy without Mn^{2+} and the linear variation of bandgap energy between CdS ($E_{g(\mathrm{CdS})}$=2.45 eV) and MnS ($E_{g(\mathrm{MnS})}$=3.4 eV), respectively [56]. The parameter c is the chemical disorder constant. By extending to what has been shown in the bulk phase, Eq. (1) is used for nanoparticles with an average diameter of 3.2 nm. The band edge energies of CdS and MnS, determined from their absorption spectra, are 2.72 and 4.7 eV, respectively. The bandgap variations with composition for particles having 3.2 nm as an average diameter with the simulated bandgap derived from various c values do not correlate. From this, it is concluded that the appearance of a minimum in the bandgap with composition is not due to chemical disorder.

In the bulk phase [57], the bandgap energy minimum has been attributed to s–d and p–d exchange interactions. An exchange interaction is known to occur in the bulk magnetic semiconductors II–VI between the d electrons of the Mn^{2+} and the band electrons. The energy bandgap was related to temperature and susceptibility by [57]

$$E_g(y,T) = \frac{E_{g(\mathrm{CdS})}AT^2}{(T+B)} + \Delta E y - b\chi(y,T)T \quad (2)$$

where $\chi(y, T)$ and T are the susceptibility of the material and temperature, respectively. A, B and b are constants. The first two depend on the material whereas the last takes into account the exchange interactions between the Mn^{2+} d electrons and band electrons. The A and B values are determined from the energy bandgap variation, at a given composition, with temperature. They are size-independent and equal to $5.6\pm0.7\times10^{-4}$ eV K^{-1} and 256±14 K, respectively. These values are close to those obtained in the bulk phase [58]. This probably indicates that the electron–phonon interactions do not markedly depend on the dot size in $\mathrm{Cd}_{1-y}\mathrm{Mn}_y\mathrm{S}$ nanocrystals.

For nanocrystals, we assume that Eq. (2) is valid. To simulate it, we use the theoretical bulk susceptibility, $\chi(y)$, as calculated by an equation given in [56]. These values are not known for nanocrystals.

To determine the b value from Eq. (2), the magnetic susceptibility, $\chi(y, T)$, in the nanoscale range and at various compositions has to be known. Unfortunately, for experimental reasons, it is impossible to determine $\chi(y)$ at 298 K. By using a SQUID, the magnetic susceptibility, $\chi(y, T)$, is measured at various temperatures, from 3 to 180 K. This is done for various particle sizes and compositions. As in the bulk phase above 60 K the magnetic susceptibility follows the Curie–Weiss law:

$$\chi(y,T) = \frac{C_0 y}{[T + \Theta_0 y]} \quad (3)$$

where $C_0 y$ and $\Theta_0 y$ are the $\mathrm{Cd}_{1-y}\mathrm{Mn}_y\mathrm{S}$ Curie constant and temperature, respectively.

At a given particle size and composition, the C_0 and Θ_0 values are deduced by plotting $\chi(T, y)^{-1}$ versus T (Fig. 8). Table 3 gives the C_0 and Θ_0 values determined for various particle sizes. Taking into account

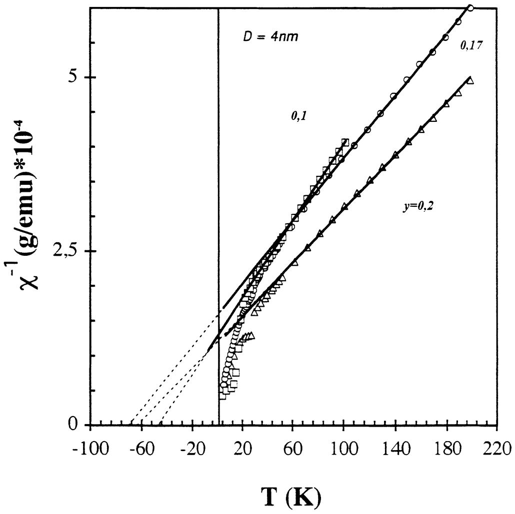

Fig. 8. Variation of the inverse magnetic susceptibility with temperature measured for 4 nm $\mathrm{Cd}_{1-y}\mathrm{Mn}_y\mathrm{S}$ nanoparticles with y=0.1, 0.17 and 0.2.

Table 3
C_0 and Θ_0 values derived from χ^{-1} extrapolation and variation of the parameter b, derived from simulation of bandgap evolution by Eq. (4) and experimental linewidth, ΔH_{pp}, of $\mathrm{Cd}_{0.9}\mathrm{Mn}_{0.1}\mathrm{S}$ nanoparticles for different sizes

	1.8 nm	3.2 nm	4 nm	Bulk
C_0 (K)	0.015	0.025	0.03	0.03
Θ_0 (emu g K^{-1})	700	630	409	280
b (eV g Oe emu^{-1} K^{-1})	1250	440	150	120
ΔH_{pp} (Gauss)	400	250	182	–

these values, the magnetic susceptibility is calculated at 298 K (Eq. (3)).

The *b* value is then deduced from the best fit (full line) between experimental data and calculation obtained from Eq. (2). Table 3 shows a drastic increase in the *b* value with decreasing particle size. This indicates an increase in the exchange interactions. Indeed, the *b* value is directly related to the interaction strength between manganese ions and conduction and valence band electrons:

$$C_0 = \frac{N_0(g\mu_B)^2 S(S+1)}{3k_B}, \qquad \Theta_0 = \frac{-(2/3)S(S+1)ZJ}{k_B} \tag{4}$$

where N_0 is the number of cations per unit volume (to a first approximation, N_0 does not depend on y in the range $0<y<0.3$), g the Lande factor, μ_B the Bohr magneton, $S=\frac{5}{2}$, k_B the Boltzman constant, Z the number of nearest neighbors (Z=12 for zinc-blende DMS) and J the nearest neighbor exchange integral ($J/k_B=-4$ K for $Cd_{1-y}Mn_yS$) [36]. Table 3 gives the calculated C_0 and Θ_0 values and the *b* value is deduced from the same procedure as described above. Table 3 shows a drastic increase of the *b* values obtained with nanocrystals.

From these data, it is concluded that an increase in the exchange interactions between the d electrons of Mn^{2+} and the band electrons will decrease the particle size.

It is well established that the Mn^{2+}–Mn^{2+} interactions occur through a superexchange process [59] which imply the CdS band electrons. As demonstrated above, the increase in the *b* factor upon decreasing the particle size involves interactions between d electrons of Mn^{2+} and the band electrons. From this, we expect to observe an increase in the Mn^{2+}–Mn^{2+} interactions. To demonstrate this, magnetization measurements are performed. The magnetic susceptibility, $\chi(y, T)$, of $Cd_{1-y}Mn_yS$ nanocrystals differing by their sizes and compositions is measured at 30 K and compared to that obtained in the bulk phase.

For particles having 4 nm as average diameter, Table 4 shows an increase in the magnetic susceptibility, $\chi(y, 30\,K)$, with increase in the composition, y. The $\chi(y, 30\,K)$ values obtained at various compositions are in good agreement to those given by Chen et al. [61], whereas they disagree with those of Yang et al. [62] (Table 4). It is impossible to measure, over the entire range, the magnetic susceptibility at various compositions for 3.2 and 1.8 nm nanocrystals. However, taking into account that magnetic susceptibility increases with composition, the values given in Table 4 permit to assume a decrease in the magnetic susceptibility upon decreasing the particle size. With $Zn_{1-y}Mn_yS$ [19] the converse behavior is obtained (decrease in $\chi(y)$, with increasing particle size).

Fig. 9 shows the EPR spectra of 4 nm $Cd_{1-y}Mn_yS$ nanocrystals, made under procedure III, recorded at various compositions ($0.006<y<0.2$) at room temperature. Each spectrum is made up of two parts:

1. A hyperfine structure with six lines on each spectrum. With an increase in manganese composition, the intensity of these peaks decreases and disappears at y=0.2.
2. A broad spectrum due to Mn–Mn interactions is observed. This spectrum fits a Lorentzian curve and the peak-to-peak linewidth, ΔH_{pp}, is deduced. The ΔH_{pp} value is deduced for various compositions, y (Table 4). The y increase leads to the broadening of the EPR line.

From these data, it is concluded that the magnetic interactions increase upon decreasing the particle size.

To be able to confirm these abnormal interaction variations we studied the Mn^{2+}–Mn^{2+} interactions through magnetic measurements recorded for different size of nanocrystals (1.8–3.2–4 nm) at various compositions ($0.006<y<0.2$). Fig. 10 shows the magnetization curves recorded at 3 and 10 K for 4 nm particles.

Table 4
$\chi_i\ 10^5$ (emu g^{-1}) values of nanoparticles at various compositions and measured at 30 K

y	Nanoparticles (nm)			Bulk phase	
	1.8	3.2	4	Chen et al. [60]	Yang et al. [61]
0.03		–	1.62	–	–
0.04		1.25	–		
0.09		–	4		–
0.1	2.64	–	4.7	4.25	–
0.17		–	5		–
0.2	–	–	6.17	4.7	–
0.22		4.92	–	–	–
0.25		–	–	–	17
0.3	–	–	–	6.1	15

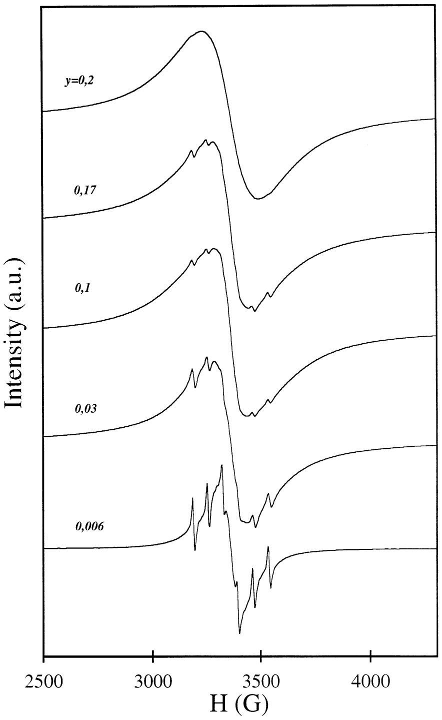

Fig. 9. EPR spectra of 4 nm $Cd_{1-y}Mn_yS$ nanoparticles prepared by procedure III and recorded at various compositions $0.006<y<0.2$, with a microwave frequency $\nu=9.43$ GHz, at room temperature and $P=10.2$ mW.

It can be noticed that saturation is reached neither at 3 K nor at 10 K. The magnetization, M, is described by the Brillouin function:

$$M = yN_0 g\mu_B S B_S \left(\frac{g\mu_B SH}{k_B T}\right) \tag{5}$$

where B_S and H are the standard Brillouin function and the applied field with $g=2.0023$.

However, because of the Mn–Mn interactions, the standard Brillouin function cannot be applied and Gaj et al. [62], proposed an empirical and phenomenological expression to describe magnetization using the effective T and S parameters:

$$M = yN_0 g\mu_B S_{\text{eff}} B_S \left(\frac{g\mu_B SH}{k_B T_{\text{eff}}}\right) \tag{6}$$

The two parameters, S_{eff} and T_{eff} deduced from the modified Brillouin function (Eq. (6)) take into account the effect of the antiferromagnetic clustering. S_{eff} is the effective mean spin of the Mn^{2+} ions and is always smaller than $\frac{5}{2}$. This is due to antiferromagnetic Mn^{2+} interactions that reduce magnetization and allow spin pair formation with a zero total magnetization. It decreases with increasing Mn^{2+} composition since the probability of magnetic ions occupying neighboring lattice sites increases.

A good agreement between the experimental data and the calculated curves is obtained by using the modified Brillouin function (Fig. 10). Some uncertainty in the exact S_{eff} values are expected because of the fact that the magnetization saturation is never reached. However, some information can be deduced from Table 5.

1. The S_{eff} values of nanocrystals are smaller than those determined in the bulk phase [60]. This indicates that the number of spins correlated in antiferromagnetic clusters is higher in nanoparticles. This means stronger Mn^{2+}–Mn^{2+} interactions in $Cd_{1-y}Mn_yS$ nanomaterials compared to the bulk phase.
2. At fixed composition, y, the S_{eff} value decreases with decreasing the particle size. Thus, interactions between spins increase with decreasing particle size.
3. For a given particle size, the S_{eff} value decreases with increasing composition. This is due to formation of spin pairs inducing antiferromagnetic Mn^{2+}–Mn^{2+} interactions.
4. The S_{eff} values decrease with decreasing temperature. This is due to the thermal motion which decreases with temperature and the spins are free to interact with their neighbors.

All these data indicate an increase in the Mn^{2+}–Mn^{2+} interactions (S_{eff}) and a decrease in the magnetic susceptibilities, $\chi(y)$, with decreasing particle size. From these data, it can be clearly concluded that the increase in the depth of the minimum of the bandgap variation with composition is due to strong interactions between manganese ions and the conduction and valence band electrons and the magnetic interactions markedly increase with decreasing particle sizes.

The PL spectra of $Cd_{0.95}Mn_{0.05}S$ nanocrystals made under procedure I, in the range of sizes from 1.8 to 3.2 nm recorded at 77 K are shown in Fig. 11. For 1.8 nm particles, the PL spectrum has a large band centered at 600 nm. This luminescence is homothetic to that obtained without Mn^{2+} ions included in-

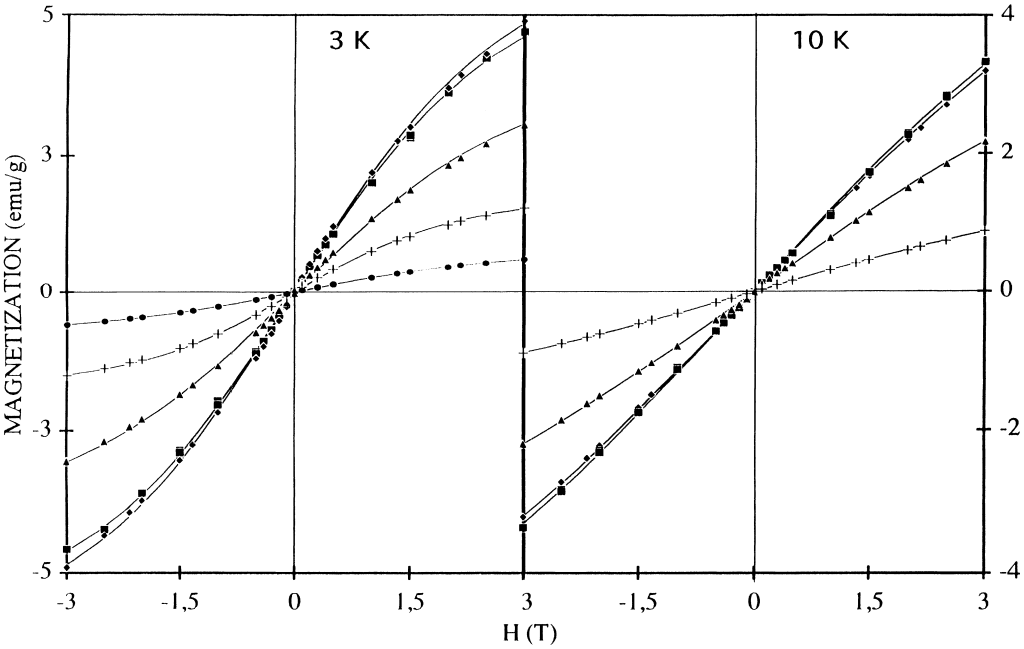

Fig. 10. Magnetization curves of 4 nm $Cd_{1-y}Mn_yS$ nanoparticles, recorded at 3 and 10 K, over compositions $0.006<y<0.2$. The solid lines are the modified Brillouin function simulations. (■) y=0.2, (◆) 0.17, (▲) 0.1, (+) 0.03, and (●) 0.006.

side the CdS matrix and is attributed to CdS defect states [5,9,18,42,43]. The photoluminescence excitation (PLE) spectrum of trap emission shows a well resolved excitonic peak (Fig. 11). A slight shift in the PLE spectra with the emission wavelength is obtained. This is due to the size distribution.

Similar behavior is observed for 3.2 nm crystallites with good correlation between the bandgap energy determined from absorption and PLE spectra. As

Table 5

S_{eff} and T_{eff} values of nanoparticles, fitting parameters, are derived from magnetization curves (the results with stars have been obtained on the bulk material by Chen et al. [61])

4 nm particles					Bulk $Cd_{1-y}Mn$ yS		
y	T (K)						
	3 K		10 K		1.5 K	5.7 K	10.9 K
	S_{eff}	T_{eff}	S_{eff}	T_{eff}	S_{eff}		
0.006	1.76	4.7	–	–	–	–	–
0.03	0.78	3.5	0.87	10	1.53	–	–
0.1	0.54	5	0.63	10	0.95	–	–
0.15	–	–	–	–	0.79	0.81	0.85
0.17	0.48	4.7	0.53	10	–	–	–
0.2	0.38	4.6	0.47	10	0.37	–	–
3.2 nm nanoparticles							
0.04	0.48	3.8	0.51	10			
0.22	0.28	4.6	0.34	10			
1.8 nm nanoparticles							
0.1	0.37	3	0.45	1			

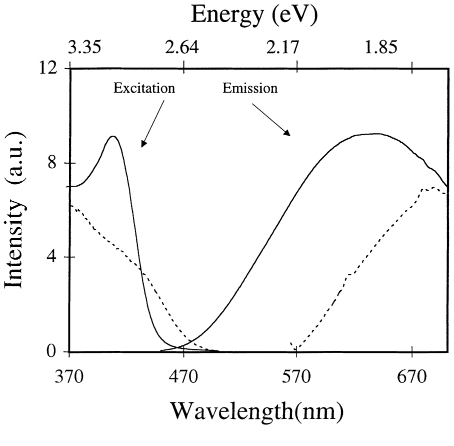

Fig. 11. PL (λ_{ex}=400 nm) and PLE (λ_{em}=600 nm) spectra, recorded at 77 K of $Cd_{0.95}Mn_{0.05}S$ nanoparticles prepared by procedure I and having various sizes: 1.8 (—) and 3.2 nm (……).

expected from Dannhauser et al. [63], the CdS traps emission is red shifted when the particle size increases. The bandgap energies are derived from the PLE spectra, and compared to those obtained from absorption spectra at the same temperature (77 K). A rather good agreement between these two techniques is observed. Hence by using procedure I the PL spectra are attributed to trap emissions of CdS nanocrystals. The presence of Mn^{2+} inside the CdS matrix does not perturb the PL spectra. This result is in total disagreement to those previously obtained [19–21].

To explain such differences between our experimental data and those published previously [19–23], syntheses modes are changed.

When 4 nm particles are made by using procedure III (w=40), the PL and PLE spectra of particles differing by their compositions are recorded at 77 K. Without Mn^{2+} included in CdS matrices, there are two luminescent bands as shown in Fig. 12A. The main luminescence band is broad and is attributed to CdS trap emission. When Mn^{2+} ions are included in a CdS matrix, the direct transition disappears and a new luminescence band with a sharp peak centered at 580 nm (Fig. 12B and C) appears. This is attributed to Mn^{2+} emission in a tetrahedral coordination (transition $^4T_1$ to $^6A_1$) [58,64]. The PL spectrum is fitted by assuming two Gaussian curves and two spectra are derived: The dashed spectrum given in Fig. 12C is characterized by a maximum centered at 585 nm and attributed to the isolated Mn^{2+} PL spectrum [26]. The simulated half-width of Mn^{2+} luminescence is 0.23 eV, which is in good agreement with that determined for Mn^{2+} luminescence in the bulk phase [26] and in $Zn_{1-y}Mn_yS$ nanoclusters [6,7,55,59]. This indicates formation of isolated manganese ions in tetrahedral site. To confirm that, EPR measurements are performed at various compositions.

The EPR spectrum is recorded at 103 K for y=0.006. The hyperfine structure deduced from the difference between the experimental spectrum and the Lorentzian fit shows six well defined intensive lines and between each of them, two weaker lines corresponding to forbidden transition with a nuclear hyperfine splitting of 69 G (Fig. 13B). This is characteristic of isolated manganese ions in CdS matrix.

Hence from the PL spectrum and the hyperfine structure, it is clearly demonstrated that the isolated Mn^{2+} are present in CdS matrix.

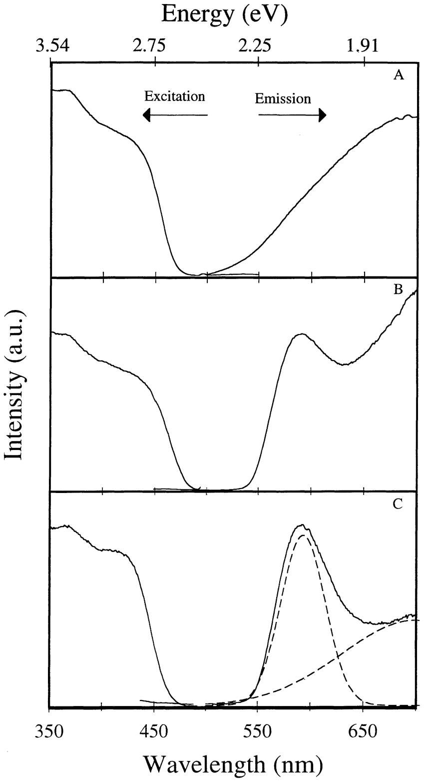

Fig. 12. PL (λ_{ex}=400 nm) and PLE (λ_{em}=580 nm) spectra, recorded at 77 K at various compositions: y=0 (A), 0.05 (B) and 0.1 (C). The average particle diameter is 4 nm. The particles are prepared by procedure III.

For CdS quantum dots [65] the PL intensity dependence with temperature obeys an Arrhenius equation as

$$\frac{I_{77\,\mathrm{K}}}{I(T)} = A'T^{-0.5}\exp\left(\frac{-E_a}{KT}\right) \tag{6}$$

where $I_{77\,\mathrm{K}}$ and I are the relative PL intensities of fluorescence recorded at 77 K and at T (K), respectively.

For $Cd_{1-y}Mn_yS$ we assume, as observed with CdS quantum dots that

1. Eq. (6) is valid for alloy semiconductor quantum dots.
2. The $Cd_{1-y}Mn_yS$ luminescence does not markedly vary below 77 K.

The activation energy, E_a, is obtained from the best fit of Eq. (4) with the experimental data for 580 and 700 nm emission wavelengths (Fig. 14). At y=0,

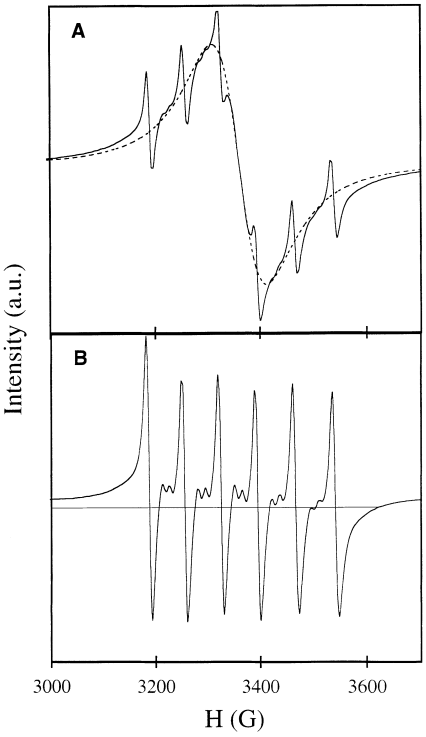

Fig. 13. (A) EPR spectra of 4 m $Cd_{99.004}Mn_{0.006}S$ nanoparticles prepared by procedure III and recorded at 103 K with a microwave frequency ν=9.43 GHz and P=10.2 mW. (B) EPR spectrum of hyperfine structure deduced from spectrum given in A.

the same activation energies are obtained at 580 and 700 nm, whereas they differ in the presence of Mn^{2+} (Table 6). This confirms the emission of two distinct centers.

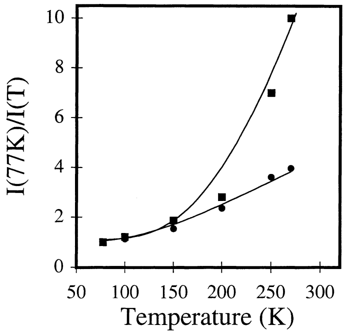

Fig. 14. Variation of the PL relative intensity obtained at 77 and T K ($I(T=77\,K)/I(T)$), with temperature. The intensities are observed at 580 (■) and 700 nm (●), respectively. The line indicates the best fit between the experimental data and Eq. (6).

Table 6
Variation of activation energy determined from evolution of luminescence band at 580 and 700 nm with temperature[a]

y	0	0.05	0.10
$E_{a(580\,nm)}$(meV)	32	60	62
$E_{a(700\,nm)}$(meV)	32	32	32

[a] The average particle diameter is 4 nm and y varies from 0 to 0.1.

Now we concentrate on the behavior of isolated Mn^{2+} ions in CdS matrix with composition, y. The increase in the PL intensity due to isolated Mn^{2+} with increasing composition is followed by a decrease for compositions above 0.1. The plot of the relative ratio of the simulated PL spectrum (1) centered at 580 nm to that of (2) 700 nm with composition (contribution of the emission due to CdS at y=0 is extracted) shows the appearance of a maximum at y=0.1 (Fig. 15). This is related to the number of isolated (without any interactions) Mn^{2+}. The number of these Mn^{2+}, y_{eff}, with composition, y, has been calculated by Kreitman et al. [66]. The y_{eff} variation with composition has a maximum around 0.1. However, the shape of the relative intensity variation with composition differs from that for y_{eff}.

EPR spectroscopy are performed in the same experimental conditions. The integral of the hyperfine structure and that of the total signal are calculated from experimental data, at various compositions

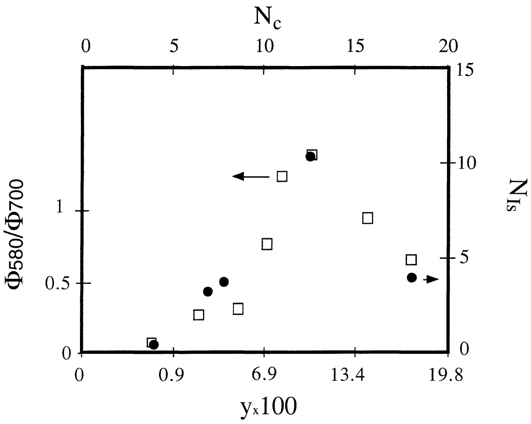

Fig. 15. Variation with composition (y) and N_C of the relative luminescence intensity (I_{580}/I_{700}) (●) and of the number of isolated Mn^{2+} per particle (☐) of the particles prepared by procedure III.

($0.006<y<0.2$). The ratio, X, of these integrals, determined at various compositions, increases with increasing composition and reaches a maximum around y=0.05 (Table 7). The number of isolated Mn^{2+}, $N_{\rm Is}$, is the product of X with composition, y, with the number of cations included in CdS particle. The latter term is estimated from Lippens et al.'s calculations [11]. The number of isolated Mn^{2+}, $N_{\rm Is}$, increases with increasing composition, y, and reaches a maximum at y=0.1. Fig. 15 shows similar variation of $N_{\rm Is}$ with composition, y, as Φ_{580}/Φ_{700}. The good correlation between the EPR hyperfine structure and the PL data shown in Fig. 15 clearly confirms that the PL is due to isolated manganese ions in a tetrahedral coordination. Hence by using procedure III isolated Mn^{2+} in tetrahedral site appears whereas from procedure I it cannot be observed.

Hence, in the nanoscale, Fig. 15 shows a progressive increase in the fluorescence yield due to isolated manganese to reach a maximum at 0.1 and then a decrease. Such a behavior markedly differs from that observed in the bulk phase where the PL [58,59] and hyperfine structure [67] of isolated Mn^{2+} ions in tetrahedral coordination are observed at low composition ($y<0.01$) [67]. The increase in Mn^{2+} content induces a disappearance in the PL intensity and a broadening of the hyperfine structure lines to reach a single line. These phenomena have been attributed to Mn–Mn energy transfer and interactions, respectively [67]. Hence, the maximum of the PL yield due to isolated Mn^{2+} ions in tetrahedral site is reached at $y<0.01$ in the bulk phase whereas it is at y=0.1 in the quantum dots. Furthermore, the relative PL quantum yield of aged particles markedly differs with aging time. To explain these differences in the behavior we take into account the process used to make the particles and particularly the resulting size and composition: As described above, for a given ratio of reactants $[Mn(AOT)_2]/([Mn(AOT)_2]+[Cd(AOT)_2])$, the composition, y, detected by EDS is always larger for particles made under procedure I than that of III. To simplify the text in the following we call Particles I and III made under procedures I and III. The slope deduced by plotting composition, y, versus $[Mn(AOT)_2]/[Mn(AOT)_2]+[Cd(AOT)_2]$ is equal to 0.86 and 0.51 for particles I and III, respectively. Particle I contains a larger amount of manganese ions compared to particle III whereas their sizes are smaller. Hence, the aging induces an increase in the particle size and a decrease in the y composition determined by EDS. Let assume that particle III (D=4 nm) is made of particle I (D=3.2 nm) surrounded by an external layer which grows during the aging (Fig. 16). Hence, particle I form the internal core with 0.4 nm thickness of an external shell. Because of the difference in composition between the particles I and III, the external phase would contain less number of manganese and could be responsible for the presence of isolated Mn^{2+} in tetrahedral site. From Lippens method [11], the total number of atoms per nanocrystal is 740 and 1400 atoms for particle I (internal core) and particle III, respectively. Then the number of cations are 370 and 700 atoms, respectively. For a given ratio of reactants in which the synthesis is made, the composition of particle I, $y_{\rm I}$, and of particle III, y, are measured by EDS. This permits to calculate the number of manganese ions in particles I and III. Hence, the number of manganese in the external layer of particle III, $N_{\rm c}$, is deduced from the difference between the number of manganese ions in particles III

Table 7
$\Delta H_{\rm pp}$, peak-to-peak distance of Lorentzian simulated curves, ratio X, integral of the hyperfine structure and total signal ratio, and $N_{\rm Is}$, ratio X multiplied by the number of Mn^{2+} ions (number of isolated ions per particles)

y	0.006	0.03	0.1	0.17	0.2
$\Delta H_{\rm pp}$ (Gauss)	90	144	180	220	210
X	0.11	0.13	0.1	0.028	–
$N_{\rm is}$	0.5	3.2	10.4	4	–

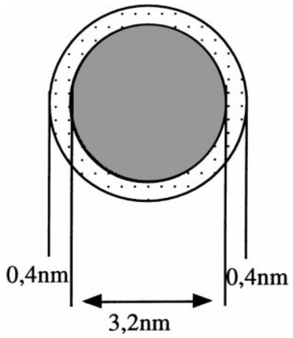

Fig. 16. Model of particles.

and I. N_c is then calculated at various compositions, y. By plotting Φ_{580}/Φ_{700} and N_{Is} versus the number of manganese ions in the external shell, N_c, a maximum is reached at N_c=12 (Fig. 15). It corresponds to a composition of particle III, y=0.1. The variation of luminescence and hyperfine structure with composition, y, and with the calculated number of isolated Mn^{2+} in the external layer, N_c, strongly supports the model shown in Fig. 16. Of course, we could expect an increase in the Mn–Mn interactions in the external layer by increasing composition. As observed in Fig. 15 above y=0.1 and/or N_c=12, the PL and hyperfine structure disappears. Hence, by assuming all the Mn^{2+} atoms are isolated in the layer, we would expect to observe a straight line by plotting the number of isolated Mn^{2+} determined by EPR versus the number of manganese atoms in the layer, N_c. Two distinct regions are observed. Below N_c=12 most of Mn^{2+} atoms in the external shell are isolated in a tetrahedral site, whereas above N_c=12, the Mn–Mn interactions are predominant and induce a decrease in the number of isolated Mn^{2+} as observed by PL and from the hyperfine structure.

The good correlation between the variation of the luminescence and the hyperfine structure of isolated Mn^{2+} with the number of atoms in the external layer formed during the aging of the particles permits to propose a model to explain the appearance of isolated Mn^{2+} ions in CdS matrix at high manganese composition compared to that observed in the bulk phase. As a matter of fact, in the bulk phase and above y=0.01, the PL spectrum decreases with increasing composition whereas such behavior is observed in the nanoscale range above y=0.1. Hence, it seems reasonable to conclude that the appearance of the PL spectrum due to isolated Mn^{2+} in CdS matrix is due to the formation of particles having an internal core rich in manganese ions which strongly interact with an external shell manganese poor and arranged in a tetrahedral structure.

So by using procedure I, no isolated Mn^{2+} ions in CdS matrix can be observed either by photoluminescence or EPR. The opposite is observed when particles are made under procedure III. It can be noticed that procedure III induces an increase in the particle size compared to I. So, these differences can be due either to a size effect or to the fabrication mode. To find out what is this effect, particles having the same average size (3 nm) have been made by following either procedure I or IV. Under procedure I, the synthesis is performed at w=40 whereas under procedure IV the synthesis is made at a water content w=10 and the particles are aging. The average particle size obtained from procedures I and IV is 2.8 and 3.2 nm, respectively. The PL spectrum of particles made under procedure I shows trap emission at room temperature (Fig. 17A) which is reinforced at 77 K (Fig. 17B). Conversely, the behavior markedly differs with particles made by using procedure IV. At room temperature, the PL spectrum is broad with a maximum centered at 680 nm and a shoulder at 600 nm (Fig. 17C). At 77 K, this behavior is reinforced with a PL spectrum characterized by a maximum centered at 590 nm (Fig. 17D). As above, two sub-spectra are derived from simulation: one centered at 585 nm, with a half width of 0.23 eV (designated 1) and the other at 650 nm (designated 2). The PL spectrum due to CdS defects and shown in Fig. 17D (number 2) is slightly red shifted compared to that obtained in Fig. 16B. This is because of the difference in the average size by using

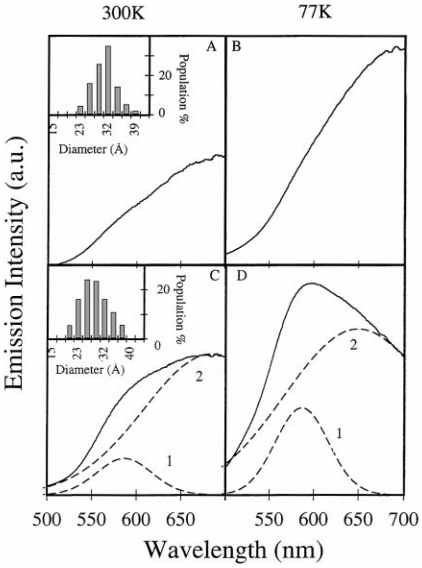

Fig. 17. PL spectra of particles prepared by procedure I (A, B) and prepared by procedure II (C, D) recorded at room temperature (A, C) and 77 K (B, D). Experimental (—) and simulated (----) spectra. Inset: Histograms of particles obtained after the various modes.

procedure I (2.8 nm) instead of procedure IV (3.2 nm). From this it seems obvious that the photoluminescence properties of $Cd_{1-y}Mn_yS$ nanocrystal depend on the preparation mode and is not size-dependent.

To confirm such behavior two other syntheses are made with particles having an average size of 4 nm. To do that, we used procedures II and IV. In both cases water content has been fixed at w=40. The average particle sizes are 4.2 and 4 nm, respectively. The PL spectrum of nanocrystals obtained from procedure IV at 250 K shows CdS trap emission. By decreasing temperature the fluorescence due to isolated Mn^{2+} appears (Fig. 18A). In contrast to procedure II, the PL spectrum (Fig. 18B), recorded at room temperature, shows a marked increase in the relative fluorescence due to isolated Mn^{2+} compared to that due to CdS defects. Hence the PL spectra of particles having similar size (4 and 4.2 nm) differ with the aging time markedly. From these data it can be concluded that the PL due to isolated Mn^{2+} ions in $Cd_{0.95}Mn_{0.05}S$ nanoclusters made in reverse micelles is observed when the particles are aged. Apparently, these data markedly differ from those obtained with $Zn_{1-y}Mn_yS$ [19–21] and $Cd_{1-y}Mn_ySe$ nanocrystallites [68,69]. A careful study of the published experimental conditions [19,20,68] clearly indicates that the luminescence due to isolated Mn^{2+} in a semiconductor matrix was observed when the particles are aged and/or have been subjected to a thermal treatment. Hence, the Mn^{2+} luminescence observed in nanoclusters, at room temperature, cannot be attributed to a quantum size effect as has been claimed previously [21].

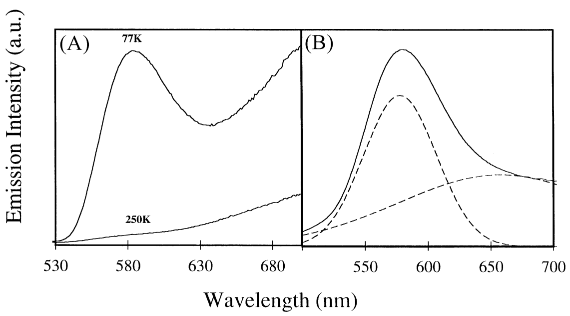

Fig. 18. (A) Room temperature and 77 K PL spectra of particles obtained by procedure III recorded at λ=400 nm. (B) Room temperature PL spectra of particles obtained by procedure II.

8. Conclusion

In this paper we demonstrate that reverse micelles can be used to make nanocrystals differing by size and compositions. Direct fluorescence can be obtained when the particles are passivated. The technique used permits to make alloys which present specific properties.

Acknowledgements

I would like to thank my coworkers who participate in this work: Drs. J. Cizeron, N. Feltin, D. Ingert, L. Levy, L.Motte and C. Petit.

References

[1] M.P. Pileni, Langmuir 13 (1997) 3266.
[2] M.P. Pileni, J. Phys. Chem. 97 (1993) 6961.
[3] I. Lisiecki, M.P. Pileni, J. Am. Chem. Soc. 115 (1993) 3887.
[4] C. Petit, P. Lixon, M.P. Pileni, J. Phys. Chem. 97 (1993) 12974.
[5] L. Motte, C. Petit, P. Lixon, L. Boulanger, M.P. Pileni, Langmuir 8 (1992) 1049.
[6] L.E. Brus, J. Chem. Phys. 79 (1983) 5566.
[7] R. Rossetti, J.L. Ellison, J.M. Bigson, L.E. Brus, J. Chem. Phys. 80 (1984) 4464.
[8] A.J. Nozik, W. Ferd, M.T. Nenadocic, T. Rajh, O.I. Micic, J. Phys. Chem. 89 (1985) 397.
[9] C. Petit, M.P. Pileni, J. Phys. Chem. 92 (1988) 2282.
[10] Y. Kayanuma, Phys. Rev. B 38 (1988) 9797.
[11] P.E. Lippens, M. Lannoo, Phys. Rev. B 39 (1989) 10935.
[12] C. Petit, P. Lixon, M.P. Pileni, J. Phys. Chem. 94 (1990) 1598.
[13] Y.Z. Hu, M. Lindberg, S.W. Koch, Phys. Rev. B 42 (1990) 1713.
[14] Y. Wang, N. Herron, Phys. Rev. B 41 (1990) 6079.
[15] M.G. Bawendi, M.L. Steigerwald, L.E. Brus, Ann. Rev. Phys. Chem. 41 (1990) 477.
[16] M.V. Rama Krishna, R.A. Friesner, J. Chem. Phys. 95 (1991) 8309.
[17] J. Nosaka, J. Phys. Chem. 95 (1991) 5054.
[18] M.P. Pileni, L. Motte, C. Petit, Chem. Mater. 4 (1992) 338.
[19] Y. Wang, N. Herron, K. Moller, T. Bein, Solid State Commun. 77 (1991) 33.
[20] R.N. Bhargava, D. Gallagher, T. Welker, J. Lumin. 60/61 (1994) 275.
[21] R.N. Bhargava, D. Gallagher, X. Hong, A. Nurmikko, Phys. Rev. Lett. 72 (1994) 416.
[22] R.N. Bhargava, J. Lumin. 70 (1996) 85.
[23] K. Sooklal, B.S. Cullum, S.M. Angel, C.J. Murphy, J. Phys. Chem. 100 (1996) 4551.

[24] A.A. Khosravi, M. Kundu, B.A. Kuruvilla, G.S. Shekhawat, R.P. Gupta, A.K. Sharma, P.D. Vyas, S.K. Kulkarni, Appl. Phys. Lett. 67 (1995) 2506.

[25] K. Yanata, K. Susuki, Y. Oka, Jpn. J. Appl. Phys. 32 (Suppl. 3) (1993) 384.

[26] Y. Oka, K. Yanata, J. Lumin. 70 (1996) 35.

[27] L. Motte, C. Petit, L. Boulanger, P. Lixon, M.P. Pileni, Langmuir 8 (1992) 1049.

[28] B.G. Potter, H. Simmons, J. Appl. Phys. 68 (3) (1990) 1218.

[29] B.G. Potter, H. Simmons, Phys. Rev. B 43 (3) (1991) 2234.

[30] B.G. Potter, H. Simmons, P. Kumar, C.J. Stanton, J. Appl. Phys. 75 (12) (1994) 8039.

[31] B.G. Potter, H. Simmons, Solid State Commun. 98 (8) (1996) 717.

[32] C.R.M. Oliveira, A.M. Paula, F.O. Plentz Filho, J.A. Medeiros Neto, L.C. Barbosa, O.L. Alves, E.A. Menezes, J.M.M. Rios, H.L. Fragnito, C.H. Brito Cruz, C.L. Cesar, Appl. Phys. Lett. 66 (4) (1995) 439.

[33] A.M. Paula, L.C. Barbosa, C.H.B. Cruz, O.L. Alves, J.A. Sanjurjo, C.L. Cesar, Appl. Phys. Lett. 69 (3) (1996) 357.

[34] L.C. Barbosa, V.C.S. Reynoso, A.M. Paula, C.R.M. Oliveira, O.L. Alves, A.F. Craievich, R.E. Marotti, C.H. Brito Cruz, C.L. Cesar, J. Noncryst. Sol. 219 (1997) 205.

[35] Y. Msumoto, K. Sonobe, Phys. Rev. B 56 (15) (1997) 9734.

[36] J.K. Furdyna, J. Kossut, Semiconductors and Semimetals, Vol. 25, Academic Press, New York, 1988.

[37] C. Petit, P. Lixon, M.P. Pileni, Langmuir 7 (1991) 2620.

[38] K.T. Higa, D.C. Harris, Organometallics 8 (1989) 1674.

[39] M.P. Pileni, Reverse Micelles, Elsevier, Amsterdam, 1989.

[40] D. Ingert, N. Feltin, L. Levy, P. Gouzert, M.P. Pileni, Adv. Mater. 11 (1999) 220.

[41] Y. Wang, N. Herron, J. Phys. Chem. 95 (1991) 525.

[42] N.A. Kotov, F.C. Meldrum, C. Wu, J.H. Fendler, J. Phys. Chem. 98 (1994) 2735.

[43] J.L. Coffer, S.R. Bigham, R.F. Pinizzotto, H. Yang, Nanotechnology 3 (1992) 69.

[44] J. Cizeron, M.P. Pileni, J. Phys. Chem. 99 (1995) 17410.

[45] J. Cizeron, M.P. Pileni, Nanostruct. Mater. 8 (1997) 419.

[46] J. Cizeron, M.P. Pileni, J. Phys. Chem. 101 (1997) 8887.

[47] L.G. Suslina, E.L. Danasyuk, S.G. Konnikov, D.L. Federov, Fiz. Tekh. Poluprovodn. 10 (1976) 1830.

[48] L. Levy, J.F. Hochepied, M.P. Pileni, J. Phys. Chem. 100 (1996) 18332.

[49] L. Levy, N. Feltin, D. Ingert, M.P. Pileni, J. Phys. Chem. 101 (1997) 9153.

[50] L. Levy, D. Ingert, N. Feltin, M.P. Pileni, Adv. Mater. 10 (1998) 53.

[51] N. Feltin, L. Levy, D. Ingert, M.P. Pileni, J. Phys. Chem. 103 (1999) 4.

[52] N. Feltin, L. Levy, D. Ingert, M.P. Pileni, Adv. Mater. 11 (1999) 398.

[53] L. Levy, N. Feltin, D. Ingert, M.P. Pileni, Langmuir 16 (1999) 3386.

[54] W. Vogel, J. Urban, M. Kundu, S.K. Kulkarni, Langmuir 13 (1997) 827.

[55] M. Ikeda, K. Itoh, S. Hisano, J. Phys. Soc. Jpn. 25 (1968) 455.

[56] C.T. Tsai, S.H. Chen, D.S. Chuu, W.C. Chou, Phys. Rev. B 54 (1996) 11555.

[57] R.B. Bylsma, W.M. Becker, J. Kossut, U. Debska, Phys. Rev. B 33 (1986) 8207.

[58] J.K. Furdyna, J. Appl. Phys. 64 (1988) R29.

[59] M. Ikeda, K. Itoh, S. Hisano, J. Phys. Soc. Jpn. 25 (1968) 455.

[60] B.E. Larson, K.C. Hass, H. Ehrenreich, A.E. Carlsson, Solid State Commun. 56 (1985) 347.

[61] C.-J. Chen, M. Qu, W. Hu, X. Zhang, F. Lin, H.-B. Hu, K.-J. Ma, W. Giriat, J. Appl. Phys. 69 (1991) 6114.

[62] Y.Q. Yang, et al., J. Sol. State Chem. 49 (1983) 20.

[63] J.A. Gaj, R. Planel, G. Fishman, Solid State Commun. 29 (1979) 435.

[64] T. Dannhauser, M. O'Neil, K. Johansson, D. Whitten, G. McLendon, J. Phys. Chem. 90 (1986) 6074.

[65] H.-E. Gumlich, J. Lumin. 23 (1981) 73.

[66] Y. Wang, N. Herron, J. Phys. Chem. 92 (1988) 4988.

[67] M.M. Kreitman, D.L. Barnett, J. Chem. Phys. 43 (1965) 364.

[68] P.B. Dorain, Phys. Rev. 112 (1958) 1058.

[69] Y. Oka, K. Yunaka, J. Lumin 70 (1996) 35.